communications materials

A Nature Portfolio journal

Article

https://doi.org/10.1038/s43246-026-01215-9

Transition-metal-doped WSe_2 homojunctions for multifunctional logic and optoelectronic devices

Check for updates

Vu Khac Dat[1,8], Minh Chien Nguyen[2,8], Hai Phuong Duong[3,8], Tien Dat Ngo[4,8], Mallesh Baithi[2], Van Dam Do[2], Chengyun Hong[5], Van Cao Nguyen[3], Thi Uyen Tran[6], Dinh Hoa Luong[3], Ki Kang Kim[3], Seong Chu Lim[2], Quynh Le-Van[1], Woo Jong Yu[2] ✉, Tuan Dung Nguyen[1] ✉ & Ngoc Thanh Duong[7] ✉

Control of carrier polarity in two-dimensional van der Waals semiconductors is essential for integrated electronic and optoelectronic systems. Here, we demonstrate that substitutional vanadium doping enables robust p-type modulation in multilayer WSe_2 with pronounced thickness-dependent transport behavior. The transfer curve of V-doped transistor reveals that increasing vanadium concentration progressively enhances hole-dominant transport, in contrast to pristine WSe_2, which evolves toward ambipolar and n-type conduction with increasing thickness. Leveraging this thickness-engineered of WSe_2/V-WSe_2 platform, we demonstrate three distinct device architectures: (i) Complementary logic inverters, (ii) flexible photovoltaic devices, and (iii) gate-programmable in-sensor imaging devices. Flexible photovoltaic homojunctions exhibit a fast response time of 1.36 μs, broadband photodetection spanning the ultraviolet to near-infrared, and a high external quantum efficiency of up to 51.3%, while maintaining stable performance under mechanical deformation. Separately, complementary inverter devices demonstrate reliable logic functionality, whereas gate-tunable homojunctions reversibly switch between negative and positive photocurrent through gate-modulated band alignment, enabling programmable in-sensor image processing. Our results establish vanadium doping as an effective strategy for carrier polarity control and for high-performance WSe_2/V-WSe_2-based homojunction electronic and optoelectronic devices.

Two-dimensional (2D) materials have emerged as promising candidates for advanced electronic and optoelectronic device applications owing to their atomically thin body geometry, strong light-matter interaction, and highly tunable electronic structures[1–5]. In addition, the absence of dangling bonds further enables the formation of high-quality van der Waals (vdWs) interfaces, allowing precise band alignment in both heterostructures and homojunctions[6]. Among 2D materials, transition-metal dichalcogenides (TMDs) exhibit pronounced thickness-dependent electronic and optical properties, providing a versatile platform for diverse optoelectronic functionalities[7–11]. While monolayer TMDs possess direct band gaps suitable for light emission[12], their limited optical absorption (~ 10%)[13,14], and enhanced surface scattering restrict performance in applications such as photodetectors and photovoltaic devices, where multilayer configurations are more favorable[4,7]. In contrast, multilayer TMDs provide enhanced absorption[7], higher current-carrying capacity[4,15], and improved stability[4,16], offering a practical pathway toward scalable optoelectronic devices. Recent studies have shown that multilayer TMDs provide a robust platform for high-performance photodetectors, achieving ultrafast response[17], broadband spectral sensitivity[18,19], and mechanical robustness through vertical carrier transport[15,20], engineered homojunctions[21,22], and asymmetric

[1]Center for Materials Innovation and Technology (CMIT), College of Engineering and Computer Science, VinUniversity, Gia Lam District, Hanoi, Vietnam. [2]Department of Electrical and Computer Engineering, Sungkyunkwan University, Suwon, Republic of Korea. [3]Department of Energy Science, Sungkyunkwan University, Suwon, Republic of Korea. [4]Imec, Remisebosweg 1, Leuven, Belgium. [5]Department of Materials Science and Engineering, Pohang University of Science and Technology, Pohang, Republic of Korea. [6]SKKU Advanced Institute of Nano Technology, Sungkyunkwan University, Suwon, Republic of Korea. [7]Faculty of Materials Science and Engineering, Phenikaa School of Engineering, Phenikaa University, Hanoi, Vietnam. [8]These authors contributed equally: Vu Khac Dat, Minh Chien Nguyen, Hai Phuong Duong, Tien Dat Ngo. ✉e-mail: micco21@skku.edu; dung.nt9@vinuni.edu.vn; thanh.duongngoc1@phenikaa-uni.edu.vn

contact designs[5,15,23]. Beyond high-speed photodetection, gate-programmable WSe_2 architectures further enable in-sensor imaging by allowing dynamic control of photoresponse polarity and responsivity at the pixel level[10,23]. Additionally, owing to its flexibility, Zou et al. reported multilayer WSe_2 photodetectors exhibiting ultrahigh responsivity and excellent mechanical stability under extreme thermal conditions[16], while Hong et al. demonstrated a vertical multilayer WSe_2 photodetector with silicon-competitive response speed and high responsivity by leveraging enhanced optical absorption and efficient vertical carrier transport[4]. However, device performance remains constrained by factors such as limited internal quantum efficiency arising from strong exciton binding energy[24–26], immature doping control[7], and defect-induced carrier trapping[27], highlighting the need for coordinated optimization of thickness engineering and doping strategies to enhance built-in electric fields and enable efficient photocarrier extraction in 2D optoelectronic devices.

Controllable carrier polarity is a key requirement for complementary logic circuits and efficient optoelectronic devices based on 2D semiconductors. Among various doping strategies, substitutional doping provides a robust, thermodynamically stable route to modulate the carrier polarity of 2D TMDs by replacing host metal atoms with aliovalent dopants, thereby enabling precise control over the Fermi-level position and transport characteristics[28–30]. Dopants with fewer valence electrons than the host metal (e.g., V or Nb substituting for W or Mo) act as acceptors and induce p-type behavior[30–32], whereas dopants with excess valence electrons (e.g., Re) introduce donor states, leading to n-type conduction[30,33]. Consequently, substitutional doping provides an effective strategy for complementary device integration in 2D semiconductors. Vanadium has emerged as an effective substitutional dopant in 2D-TMD materials owing to its favorable electronic configuration and chemical compatibility with the host lattice[34–37]. With one fewer valence electron than group-VI transition metals and a comparable covalent radius, vanadium can readily substitute metal lattice sites and act as an efficient acceptor dopant, enabling p-type transistor operation, tunable electronic and optical properties[34,38], and the emergence of dopant-induced magnetic behavior in WSe_2[39–42]. To date, most studies on V-doped TMDs have focused on monolayer-based devices, where vanadium incorporation has been optimized to control carrier polarity[35,43,44], band structure[34], and induce device functionalities[29,45,46]. In addition, V doping in monolayer WS_2 and MoS_2 enables continuous modulation of carrier polarity and enhances electrical conductivity for complementary logic applications[30,44]. However, the focus on monolayers has limited the exploration of V-doped multilayer and bulk TMDs, whose optoelectronic potential remains largely unexploited despite their advantages in optical absorption, carrier transport, and environmental stability. For practical photodetectors and photovoltaic devices, multilayer TMDs are inherently more suitable, as efficient light harvesting and robust carrier collection are essential for high-performance operation[7]. Extending vanadium doping strategies to multilayer TMDs is therefore essential, as it enables thickness-tolerant p-type modulation, reliable p-n homojunction formation, and the establishment of built-in electric fields necessary for efficient photocarrier separation. Such controlled vanadium doping in multilayer TMDs opens a viable pathway toward high-performance device functionalities that surpass the intrinsic limitations of monolayer-based devices.

In this study, we demonstrate thickness-dependent p-type WSe_2 enabled by substitutional vanadium doping and investigate its implementation for integrated optoelectronic device applications. V-doped WSe_2 crystals with controllable V atomic incorporation are realized across a wide range of multilayer thicknesses. In WSe_2, vanadium doping provides a robust and thickness-dependent route to p-type behavior, while pristine regions naturally evolve toward n-type or ambipolar transport, allowing deterministic p–n junction formation without changing the host crystal[9,39]. Exploring WSe_2 homojunctions by integrating pristine and V-doped WSe_2 within a single material platform is essential for advancing multifunctional two-dimensional electronics and optoelectronics. By leveraging this well-defined electrical modulation, we constructed pristine WSe_2/ V-doped WSe_2 homojunctions and demonstrated three representative device configurations to achieve different functionalities. First, lateral homojunction architectures are implemented as logic inverters, demonstrating complementary logic operations enabled by controlled carrier polarity. Second, homojunctions with identical thicknesses are configured as flexible photovoltaic devices, in which the built-in electric field facilitates efficient photocarrier separation and collection. Kelvin probe force microscopy (KPFM) directly visualizes the built-in electric potential at the homojunction interface, confirming effective p-n junction formation, while the devices exhibit fast photoresponse, broadband spectral sensitivity, and high external quantum efficiency. Third, gate-tunable homojunction devices are engineered to reversibly switch between negative and positive I_{ph} responses via gate-modulated band alignment, enabling programmable in-sensor image processing. Together, these device configurations highlight the versatility of V-doped WSe_2 homojunctions for diverse electronic and optoelectronic applications.

Results and discussion

Pristine and V-doped WSe_2 growth and characterization

The pristine and V-doped WSe_2 single crystals were synthesized by a two-step chemical vapor transport (CVT) strategy, in which a controlled temperature gradient drives material transport from the hot zone to the cold zone. I_2 was employed as the transport agent, enabling efficient vapor-phase transport of both W and V species without the need for salt treatment. The salt-free approach yields high-quality single crystals, as illustrated in Fig. 1a and described in the Method section. The V concentration corresponds to the nominal V: W precursor ratio used prior to growth, with the formula $V_xW_{1-x}Se_2$. The X-ray diffraction measurements reveal a systematic shift of the (002) peak toward higher angles with increasing V concentration accompanied by a monotonic reduction in the interlayer spacing *d*, indicating lattice contraction along the *c*-axis due to substitutional V incorporation (Fig. 1b). This contraction is attributed to enhanced interlayer interactions arising from free holes introduced by V dopants, which strengthen electron–electron interactions in substitutionally V-doped WSe_2 in the absence of V intercalation. Raman spectroscopy further confirms that the overall lattice symmetry of WSe_2 is preserved upon V doping (Fig. 1c), as evidenced by the retention of the characteristic A_1g and 2LA(M) modes with minor spectral changes across different V concentrations, as detailed in Supplementary Fig. 1. X-ray photoelectron spectroscopy was also used to provide direct chemical evidence for successful V substitution, with clear Se 3 d and W 4 f core-level features retained and the emergence of V 2p signals in doped samples, without signatures of secondary phases or metallic V clusters (Fig. 1d).

The atomic structure of the exfoliated V-doped WSe_2 monolayer was investigated by annular dark-field scanning transmission electron microscopy (ADF-STEM) (Fig. 1e). The atomic-resolution image reveals isolated V atoms substituting for W lattice sites, as evidenced by low-intensity contrast (green) at positions normally occupied by W atoms. Atomic-scale analysis was performed at five different regions to quantify the relative densities of vacancies and substitutional V atoms at W sites, as shown in Supplementary Fig. 2. Furthermore, the corresponding line-profile analysis shows good agreement with simulated ADF contrast, providing direct confirmation of substitutional V doping at the atomic scale.

Evolution in electrical transport of thickness-engineered Pristine and V-doped WSe_2 transistors

The electrical transport properties of pristine and V-doped WSe_2 were systematically investigated using back-gated field-effect transistor (FET) devices to elucidate the effects of thickness and vanadium concentration on carrier polarity. Figure 2 illustrates the evolution of electrical transport in pristine and V-doped WSe_2 as a function of thickness and V concentration. The corresponding optical micrograph and atomic force microscopy (AFM) images of the FET devices are shown in Supplementary Figs. 3–8. The transfer-curve measurements were carried out at a fixed drain-source bias (V_{DS}) of 3 V. The transfer characteristics measured at a lower V_{DS} of 1 V, as shown in Supplementary Fig. 9, exhibit behavior consistent with

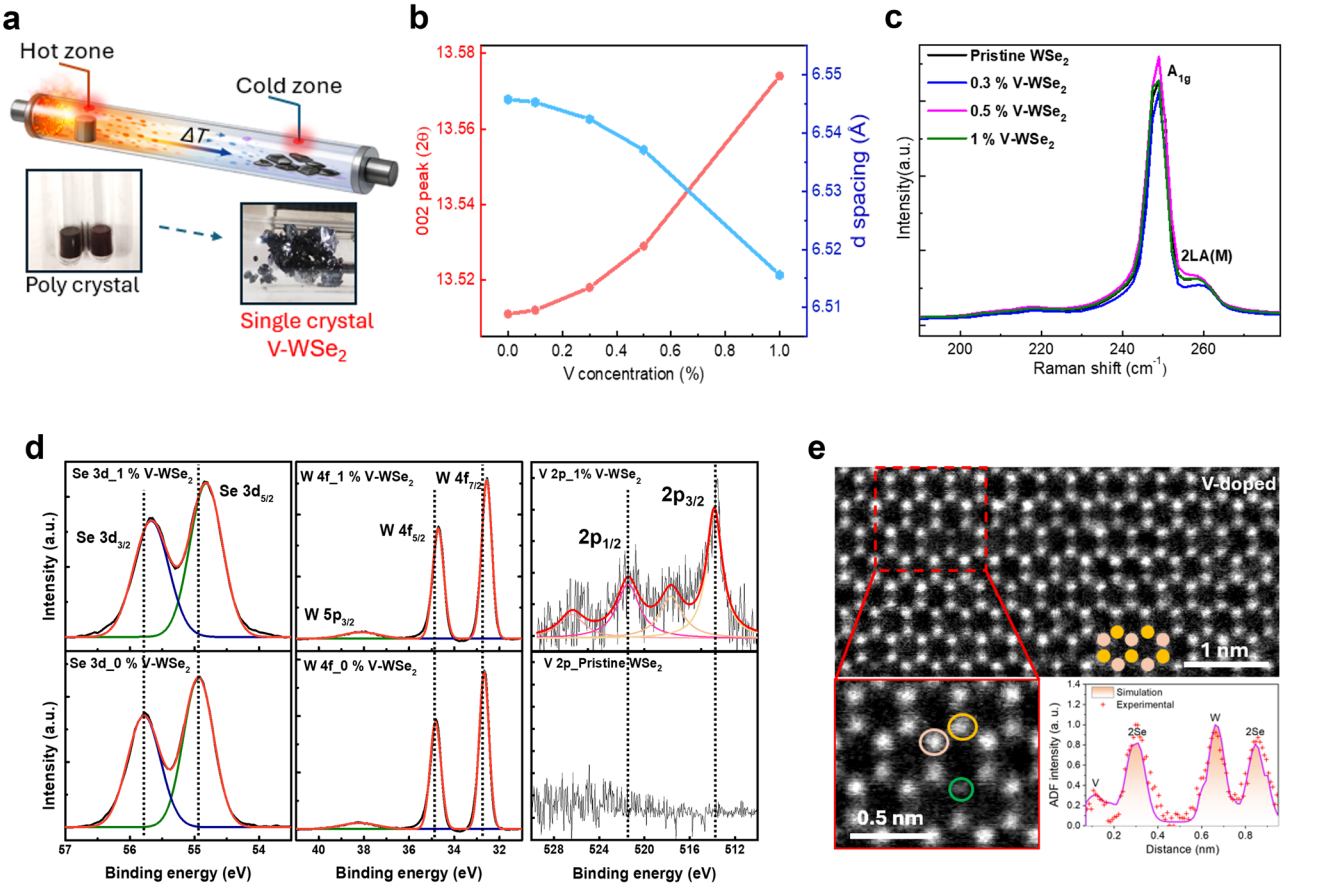


Fig. 1 | Structural characterization of pristine and V-doped WSe_2 single crystal. **a** Schematic illustration of the two-zone chemical vapor transport (CVT) growth process used to synthesize pristine and V-doped WSe_2 single crystals. **b** Evolution of the (002) X-ray diffraction peak position and the corresponding interlayer spacing (*d*) as a function of vanadium doping concentration, indicating lattice contraction along the *c*-axis upon V incorporation. **c** Raman spectra of pristine and V-doped WSe_2, showing the characteristic A_{1g} and 2LA(M) modes with minor shifts upon doping, confirming preservation of the crystal structure. **d** X-ray photoelectron spectroscopy (XPS) spectra of the Se 3 d, W 4 f, and V 2p core levels for pristine and 1% V-doped WSe_2, evidencing successful substitutional V incorporation without secondary phases. **e** Atomic-resolution annular dark-field scanning transmission electron microscopy (ADF-STEM) image of V-doped WSe_2, together with the corresponding line-profile analysis, confirming substitutional vanadium atoms at tungsten lattice sites.

those obtained at $V_{DS} = 3$ V. As shown in Fig. 2a, pristine WSe_2 devices exhibit a clear thickness dependence on their transfer characteristics. Thinner pristine WSe_2 flakes exhibit more predominantly p-type transport. As thickness increases, ambipolar behavior gradually emerges, followed by increasingly dominant electron conduction in thicker flakes. The thickness-dependent evolution of carrier polarity originates from intrinsic changes in the electronic structure of WSe_2, including bandgap narrowing and thickness-dependent shifts of the band edges, which modify their alignment relative to the Fermi level. In addition, donor-like selenium vacancy states become increasingly effective in thicker layers, shifting the Fermi level toward the conduction band and driving n-type transport. In contrast, V-doped WSe_2 exhibits a transition toward hole-dominated transport. At relatively low V-doped concentrations (0.3% and 0.5%; Fig. 2b, c), ambipolar behavior is markedly suppressed over the entire thickness range, accompanied by a positive shift in threshold voltage, confirming effective p-type modulation. At higher V concentration (1–5%; Fig. 2d–f), the devices exhibit a pronounced p-type behavior, with the electron conduction branch eliminated. Notably, in V-doped WSe_2, increasing thickness enhances the hole density, thereby reinforcing hole-dominated transport rather than promoting ambipolar behavior. These results demonstrate that the p-type transport characteristics of V-doped WSe_2 are jointly governed by vanadium concentration and layer thickness. Increased flake thickness enhances dopant incorporation efficiency and substitution probability, leading to a higher effective V concentration in thicker WSe_2 layers. However, achieving a perfectly uniform dopant distribution in multilayer WSe_2 remains challenging. Local variations in vanadium concentration may lead to spatially nonuniform electrical characteristics. For ultrathin flakes < 5 nm, Fig. 2a–c, V-doped WSe_2 exhibits electrical behavior nearly similar to pristine WSe_2, indicating that the dopant concentration is below the threshold required to significantly influence carrier transport or that a portion of the dopants remains electrically inactive. In thick flakes, with certain flakes exhibiting stronger p-type behavior than others, this effect is evident in Fig. 2f, where devices fabricated with 16- and 21-nm thick samples exhibit nearly identical conductivities, whereas a thicker flake of 26 nm shows a markedly different conductivity.

To quantitatively evaluate the electrical performance of V-doped WSe_2, we systematically extracted the field-effect mobility (μ_{FE}), threshold voltage (V_{th}), and on/off current ratio across a wide range of flake thicknesses and vanadium concentrations, as summarized in Supplementary Fig. 10. The results reveal a clear doping-dependent transport behavior. Pristine WSe_2 exhibits relatively low mobility (< 2 $cm^2 V^{-1} s^{-1}$) and strong thickness dependence, while moderate V doping (0.5–1%) significantly enhances carrier transport, yielding peak mobilities of ~10 $cm^2 V^{-1} s^{-1}$ with minimal thickness sensitivity. Concurrently, the on/off ratio improves at low-to-moderate doping (up to ~10^7–10^8) but degrades at higher doping concentrations (≥ 3%) due to increased off-state leakage and reduced gate modulation. The threshold voltage systematically shifts toward more positive values with increasing V concentration, confirming effective p-type doping via substitutional vanadium incorporation. At higher doping levels, the devices approach degenerate behavior, resulting in diminished

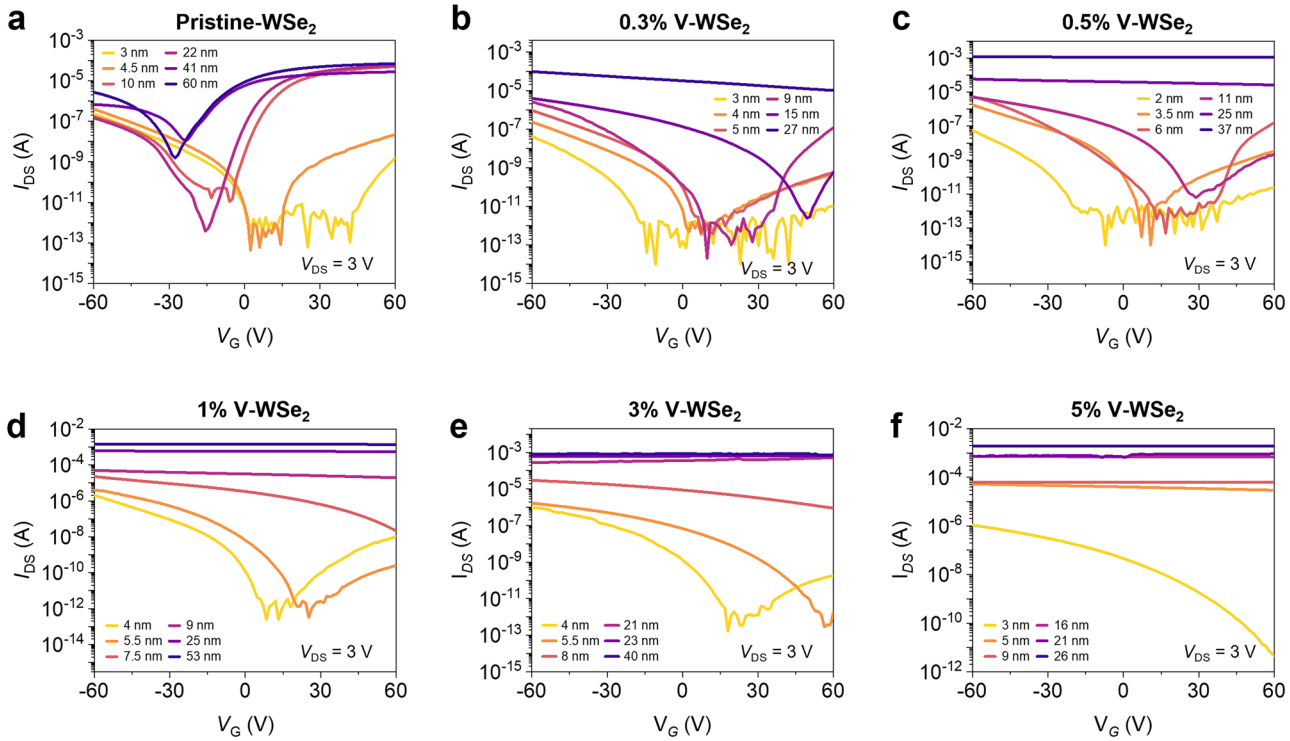


Fig. 2 | Thickness-dependent transfer characteristics of pristine and V-doped WSe_2. **a** Transfer characteristics of pristine WSe_2 field-effect transistors with varying thicknesses, showing a gradual evolution from p-type to ambipolar and increasingly n-type transport as the thickness increases. **b–f** Transfer characteristics of V-doped WSe_2 devices with vanadium concentrations of 0.3%, 0.5%, 1%, 3%, and 5%, respectively, measured at different thicknesses. In contrast to pristine WSe_2, V-doped WSe_2 exhibits suppressed ambipolar behavior and increasingly dominant p-type transport with higher vanadium concentrations. Notably, hole-dominated transport is further strengthened with increasing layer thickness, highlighting the thickness-tolerant nature of substitutional vanadium doping.

switching characteristics and less well-defined threshold voltages. These combined trends identify an optimal doping window (~ 0.5–1%), where enhanced mobility, high on/off ratio, and stable threshold behavior are simultaneously achieved, highlighting the robustness and tunability of V-doped WSe_2 for electronic and optoelectronic applications.

Homojunction-based CMOS-like inverter using pristine and V-doped WSe_2 transistors

To evaluate the potential of V-doped WSe_2 for integrated logic applications, we constructed a complementary metal-oxide-semiconductor (CMOS) inverter by integrating a p-type V-doped WSe_2 (p-FET) and an n-type pristine WSe_2 FET (n-FET) on the same substrate. As illustrated in the schematic and circuit diagram in Fig. 3a, the 0.5% V-doped serves as the p-FET, while the pristine WSe_2 acts as the n-FET. The transfer curves of the individual pristine and V-doped WSe_2 devices are shown in Supplementary Fig. 11. Both FETs share a common Si/SiO_2 back-gate, which serves as the input voltage terminal (V_{in}), with the drain supply voltage (V_{dd}) applied to the p-FET source, and the source of the n-FET is grounded (GND). The voltage transfer characteristics of the inverter are shown in Fig. 3b for various V_{dd} from 1 V to 5 V. The device exhibits clear logic inversion, with full output-voltage swing across the entire V_{dd} range, confirming effective complementary operation enabled by the controlled carrier polarity of pristine and V-doped WSe_2. The well-defined transition regions indicate a robust switching behavior and minimal noise margin. As shown in Fig. 3c, the voltage gain (dV_{in}/dV_{out}) increases with the V_{dd}, with the switching threshold shifting slightly as a function of V_{dd}. The sharp peaks in the gain profiles confirm high sensitivity in the transition region, which is essential for maintaining signal integrity in complementary logic circuits. Furthermore, we analyzed CMOS power consumption in Fig. 3d. The peak power consumption scales from approximately 18 nW at V_{dd} = 1 V to roughly 35 nW at V_{dd} = 5 V. These results establish V doping as a powerful strategy for realizing high-performance, low-power homojunction-based electronic devices and logic gates using two-dimensional (2D) semiconductors.

Flexible vdWs pristine/V-doped WSe_2 p–n homojunction

Two-dimensional materials have emerged as promising platforms for flexible optoelectronic devices. To further investigate the potential of V-doped WSe_2 for flexible photovoltaic applications, we fabricated flexible photovoltaic devices based on pristine and V-doped WSe_2 homojunctions with an intentionally selected layer thickness. To isolate the effect of vanadium-induced band modulation from thickness-related electrostatic variations, the pristine and V-doped WSe_2 regions were deliberately selected to have identical thicknesses[47,48].

Figure 4a, b shows the optical microphotograph and schematic illustration of the pristine/0.5% V-doped WSe_2 homojunction device fabricated on a flexible mica substrate (see Methods). The device was secured with adhesive tape to facilitate controlled bending during electrical and optoelectronic measurements. AFM image (Fig. 4c) confirms that both the pristine-WSe_2 and 0.5% V-doped WSe_2 possess nearly identical thicknesses of approximately 10 nm. At this thickness, pristine WSe_2 exhibits electron-dominant transport, while V-doped WSe_2 displays hole-dominant behavior at gate voltage (V_G) of 0 V, thereby enabling the formation of a p-n homojunction. This thickness regime also ensures strong optical absorption exceeding 50% with minimal reflection, thereby favoring efficient photovoltaic operation[49]. The cross-sectional scanning transmission electron microscopy (STEM) of the device is shown in Supplementary Fig. 12, indicating vdWs interface between the 0.5% V-doped WSe_2 and pristine WSe_2. To directly probe the formation of a built-in potential at the 0.5% V-doped / pristine WSe_2 interface, KPFM measurements were performed, as shown in Fig. 4d. The work-function (WF) difference between pristine WSe_2 and 0.5% V-doped WSe_2 can be estimated from the measured contact potential difference (CPD) using the relation: $\phi_{Sample} = \phi_{Tip} - \Delta_{CPD}$, where ϕ_{Sample} and ϕ_{Tip} are the WF of the sample and WF of the tip, respectively[50].

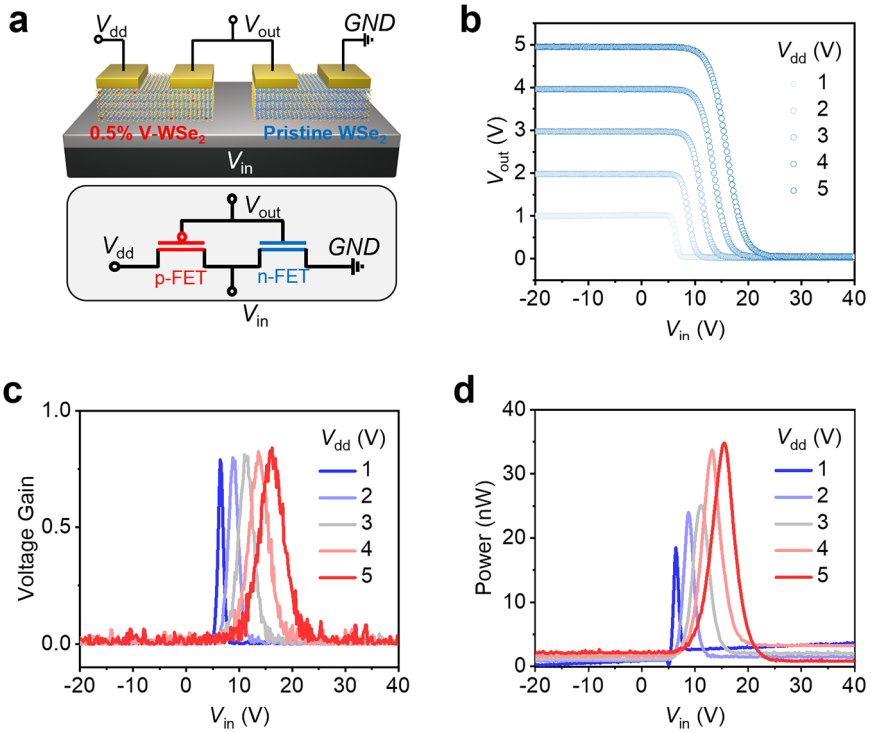


Fig. 3 | Homojunction-based CMOS-like inverter using pristine and V-doped WSe_2. a Schematic illustration (top) and equivalent circuit diagram (bottom) of the complementary metal-oxide-semiconductor (CMOS) inverter, employing 0.5% V-doped WSe_2 as the p-type field-effect transistor (p-FET) and pristine WSe_2 as the n-type field-effect transistor (n-FET). **b** Voltage transfer characteristics of the inverter, showing full-swing logic inversion for V_{dd} ranging from 1 to 5 V. **c** Corresponding voltage gain ($|dV_{out}/dV_{in}|$) extracted from the transfer characteristics, exhibiting pronounced gain peaks near the switching threshold. **d** Power consumption of the inverter during switching as a function of V_{dd} (1–5 V).

According to this relation, a lower measured surface potential corresponds to a higher sample WF. As shown in Fig. 4e and Supplementary Fig. 13, before contact, the CPD of the 0.5% V-doped WSe_2 region is approximately 0.38 eV lower than that of pristine WSe_2. This indicates that V doping increases the WF of WSe_2 and shifts its Fermi level downward toward the valence band, consistent with enhanced p-type behavior. When the pristine and V-doped regions are brought into contact, charge redistribution occurs across the interface until the Fermi levels become aligned. This equilibration results in band bending and establishes a built-in electric field at the homojunction interface. To further verify the formation of a built-in potential in the WSe_2 homojunction, spatially resolved I_{ph} mapping measurements were performed at $V_{DS} = 0$ V, as shown in Fig. 4f. The excitation laser was focused on a spot size of approximately 1 μm. The resulting I_{ph} is predominantly localized at the 0.5% V-doped/ pristine WSe_2 overlap region, indicating that the built-in electric field at the homojunction efficiently drives photocarrier separation via a photovoltaic mechanism.

Broadband photovoltaic response of pristine/V-doped WSe_2 vdWs p-n homojunctions

The power- and wavelength-dependent measurements were conducted to further elucidate the photoresponse characteristics of the flexible WSe_2 homojunction photovoltaic device. Figure 5a presents the output characteristics under 458 nm laser illumination, with incident power densities ranging from 0.22 to 2.69 nW μm^{-2}. The output characteristics of the device measured under 375 and 811 nm laser illumination are shown in Supplementary Fig. 14. Both the drain current and short-circuit current (I_{SC}) increase monotonically with increasing illumination intensity, reflecting efficient photogeneration, carrier separation, and transport of electron-hole pairs across the homojunction. To quantitatively analyze the photoresponse, the I_{ph} at $V_{DS} = 0$ V was extracted. The I_{ph} is defined as $I_{ph} = I_{SC} - I_{dark}$, where I_{SC} and I_{dark} indicate the drain current under illuminated and dark conditions, respectively. As shown in Fig. 5b, the I_{ph} exhibits a near-linear dependence on incident power density, following the relation $I_{ph} \approx P^{\alpha}$, with $\alpha \approx 1.02$. The linear scaling indicates that the I_{ph} generation is dominated by a photovoltaic mechanism rather than photoconductive gain. Notably, the device achieves a photocurrent-to-dark-current ratio exceeding 1×10^5 at zero bias, demonstrating a high signal-to-noise ratio and efficient junction-assisted carrier separation. Additional 0.5% V-doped/ pristine WSe_2 homojunction devices are shown in Supplementary Fig. 15 and exhibit performance comparable to that of the representative device shown in the main text, thereby confirming the reproducibility of the fabrication process and device characteristics.

The mechanical robustness of the device is evaluated under bending conditions, as shown in Fig. 5c, which presents the output characteristics of the flexible 0.5% V-doped/ pristine WSe_2 homojunction measured in the dark and under illumination. The photovoltaic performance remains nearly unchanged after bending, indicating that both the built-in electric field and the interfacial band alignment of the vdWs homojunction are preserved under mechanical deformation. Time-resolved I_{ph} measurements at $V_{DS} = 0$ V before and after bending are shown in Supplementary Fig. 16, indicating the stable switching under repeated light on/off cycles, with negligible change in I_{ph} amplitude after mechanical deformation. This mechanical stability is attributed to the ultrathin device architecture, with a total thickness below 100 nm, which enables efficient strain accommodation and minimizes mechanical stress during bending. Under 458 nm illumination with an incident power density of 0.88 nW μm^{-2}, the device exhibits an open-circuit voltage (V_{OC}) of 0.35 V and $I_{SC} = 75.8$ nA, extracted directly from the illuminated output curve after the mechanical bending. The fill factor (FF), defined as $FF = V_m \cdot I_m / V_{OC} \cdot I_{OC}$, where V_m and I_m correspond to the voltage and current at the maximum power point, is calculated to be 0.365. The resulting power conversion efficiency (PCE) is determined using $PCE = V_{OC} \cdot I_{OC} \cdot FF / P_{in}$, yielding 1.66%, where P_{in} denotes the incident optical power on the active device area.

The device design highlights the intrinsic role of V-induced band modulation in governing the photovoltaic behavior of WSe_2 homojunctions. Figure 5d schematically illustrates the band alignment and photocarrier separation mechanism in the 0.5% V-doped/ pristine WSe_2 homojunction under illumination. Substitutional V doping shifts the Fermi level of WSe_2 toward the valence band, forming a p-type region adjacent to pristine WSe_2. As revealed by KPFM, a band offset of approximately 0.38 eV is established at the interface (Fig. 4e), generating a built-in electric field across the homojunction that enables photovoltaic operation without an external bias. This internal field drives photogenerated electrons toward the pristine WSe_2 side and holes toward the V-doped WSe_2 side, facilitating

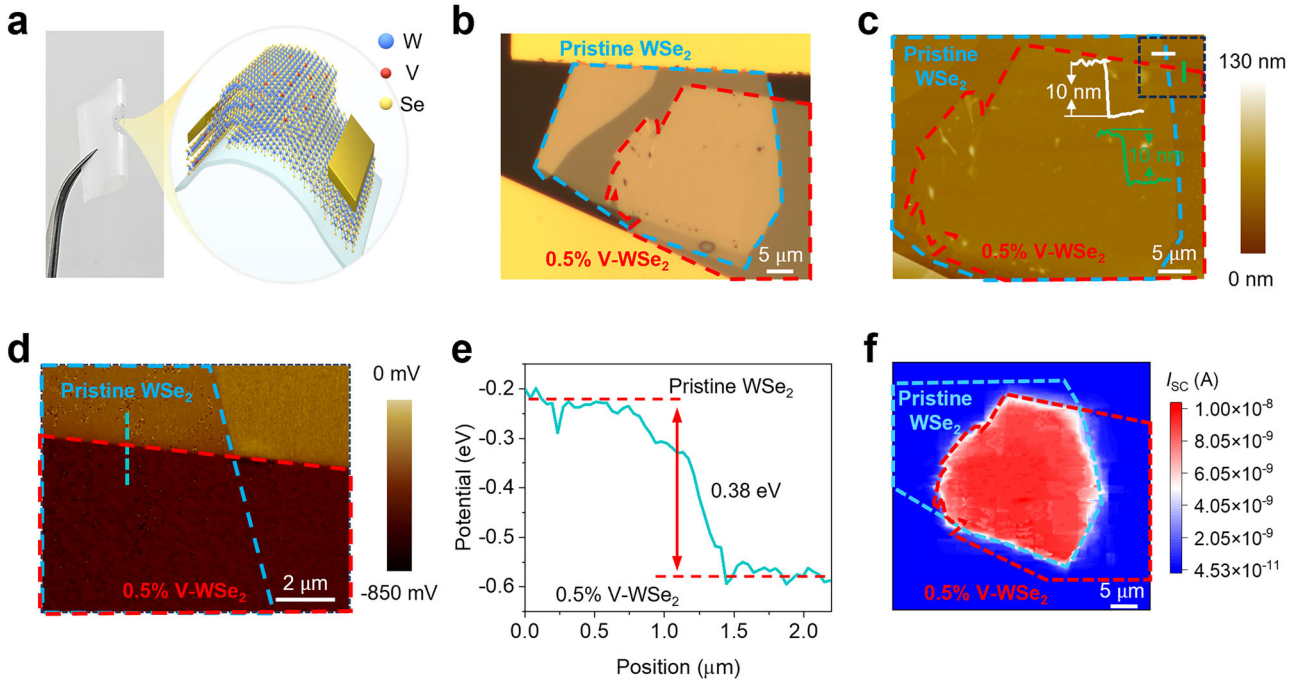


Fig. 4 | Flexible van der Waals p–n homojunction based on pristine and V-doped WSe_2. **a** Photograph and schematic illustration of the flexible 0.5% V-doped/pristine WSe_2 homojunction device fabricated on a mica substrate. **b** Optical microscopy image and **c** atomic force microscopy (AFM) topography of the device. The dashed outlines mark the pristine WSe_2 (blue) and 0.5% V-doped WSe_2 (red) regions. Height profiles extracted along the indicated lines confirm that the pristine and V-doped WSe_2 regions have comparable thicknesses (~ 10 nm). **d** Kelvin probe force microscopy (KPFM) surface potential map of the 0.5% V-doped/pristine WSe_2 homojunction. **e** Surface potential profile extracted along the dashed line in (**d**), revealing a built-in potential difference of approximately 0.38 eV between the pristine and V-doped WSe_2 regions at identical thickness. **f** Spatially resolved I_{ph} mapping measured at $V_{DS} = 0$ V under 532 nm laser illumination, showing that the I_{ph} is predominantly localized at the pristine/V-doped WSe_2 junction, confirming the homojunction as the active photoresponse region.

efficient photocarrier separation. The broadband spectral photoresponse of the device is shown in Fig. 5e, which presents time-resolved I_{ph} measurements at different wavelengths. The device exhibits a stable photoresponse across a wide spectral range, from the ultraviolet (375 nm) to the near-infrared (1062 nm), demonstrating broadband photodetection capability. The wavelength-dependent responsivity and external quantum efficiency (EQE) are extracted (Fig. 5f, g). Responsivity is calculated using $R = I_{ph}/P{\cdot}S$, where S denotes the active area. The EQE is determined from the responsivity according to the formula $EQE = R{\cdot}h{\cdot}c/\ e{\cdot}\lambda$, where h is Planck's constant, c is the speed of light, and λ is the incident laser wavelength. The device achieves a high responsivity of 155.31 mA W^{-1} and a peak EQE of 51.3% at 375 nm, reflecting efficient photocarrier conversion enabled by the homojunction. Figure 5h shows the device's fast photoresponse measured at 458 nm. At $V_{DS} = 0$ V, where I_{ph} generation is governed by the photovoltaic effect, the device exhibits a fast rise time of 1.56 μs and a delay time of 1.36 μs. The frequency-dependent I_{ph} response of the device over 1-50 kHz (Supplementary Fig. 17) shows stable, consistent I_{ph} amplitudes across all measured frequencies. The combination of high responsivity, high EQE, rapid response speed, and broadband spectral sensitivity highlights the suitability of V-doped WSe_2 for homojunction devices in high-speed, broadband optoelectronic applications.

Demonstration of in-sensor imaging with pristine/V-doped WSe_2 homojunction

We further investigate the potential of the pristine/V-doped WSe_2 homojunction for advanced optoelectronic applications, specifically in-sensor imaging, by exploiting gate-controlled modulation of band alignment. Figure 6a, b illustrates the operating concept in which the photoresponse polarity and magnitude of individual devices can be electrostatically programmed by the V_G. In this architecture, an array of devices is organized into a 3×3 matrix, referred to as a convolution kernel, where each device serves as an independently programmable sensing element (pixel). By applying appropriate gate biases, the photoresponsivity of each device within the kernel can be modulated in both magnitude and polarity. The gate-controlled switching between positive and negative I_{ph} (PPC and NPC) enables the encoding of signed photoresponsivity values essential for image-processing functions, which is demonstrated here using a degenerate V-doped/pristine WSe_2 homojunction operating as a single programmable pixel within a convolution kernel. The electronic asymmetry enables continuous modulation of the interfacial band alignment by the V_G. At a critical V_G of approximately −27 V, the band bending approaches a quasi-flat condition, minimizing I_{ph} generation, while V_G applied above or below this value induce opposite band bending due to the asymmetric gate response of the degenerate V-doped and pristine WSe_2 regions, thereby reversing the direction of photocarrier separation and enabling reversible switching between NPC ($V_G < -27$ V) and PPC ($V_G > -27$ V).

The optical image of the fabricated 0.5% V-doped/ pristine WSe_2 homojunction device is shown in Fig. 6c, with the corresponding AFM results shown in Supplementary Fig. 18. At a thickness of approximately 52 nm, the 0.5% V-doped multilayer WSe_2 exhibits degenerate p-type behavior, as evidenced by its transfer characteristics (Supplementary Fig. 19). Figure 6d shows the semilogarithmic output characteristics of the homojunction measured in the dark at different V_G. A continuous reversal of rectification polarity is observed as V_G is swept from −40 to 40 V, indicating gate-controlled modulation of the interfacial band bending and band alignment. Under laser illumination, the output characteristics shown in Fig. 6e reveal a gate-controlled transition between NPC and PPC at $V_G = -27$ V. Figure 6f shows the gate-dependent responsivity, extracted from the I_{ph} measured at $V_{DS} = 0$ V (Supplementary Fig. 20), which defines the programming voltage. The power-dependent photoresponse of the device, shown in Supplementary Fig. 21, exhibits a linear dependence on incident optical power.

To demonstrate in-sensor image processing, simulations were performed using experimentally measured responsivity values from the V-

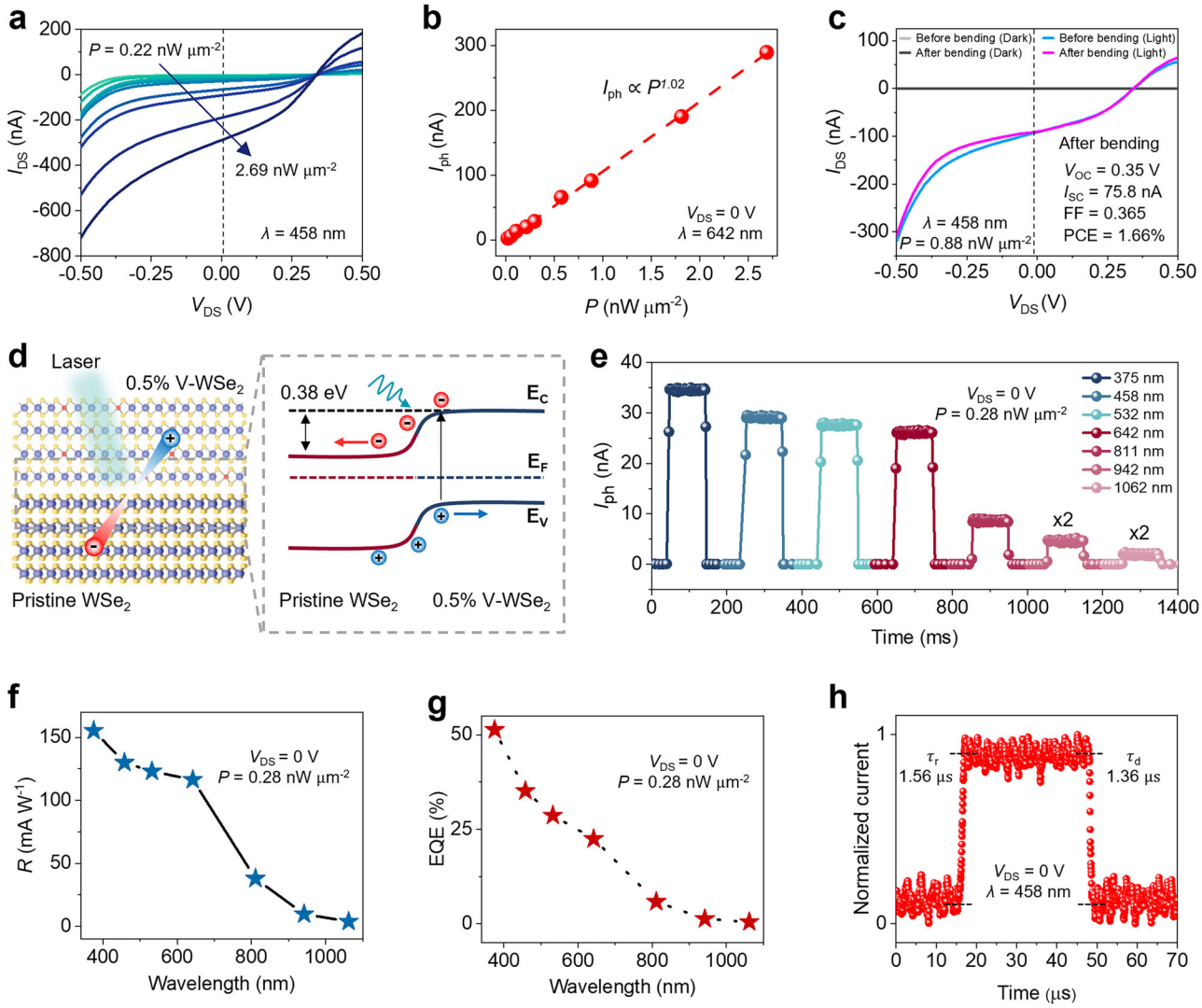


Fig. 5 | Photovoltaic response and broadband photodetection of pristine/V-doped WSe_2 van der Waals p–n homojunctions. a Output characteristics of the flexible 0.5% V-doped/pristine WSe_2 photovoltaic device measured under 458 nm illumination at different incident power densities. **b** Short-circuit current (I_{SC}) as a function of incident optical power density, showing a near-linear dependence indicative of photovoltaic operation. **c** Output characteristics of the flexible homojunction device measured before and after mechanical bending, both in the dark and under illumination, demonstrating robust photovoltaic performance under mechanical deformation. **d** Schematic energy band diagram of the pristine/V-doped WSe_2 homojunction, illustrating the built-in electric field (~ 0.38 eV) that drives photocarrier separation. **e** Wavelength-dependent I_{ph} response measured at $V_{DS} = 0$ V, together with the corresponding (**f**) photoresponsivity (R) and **g** external quantum efficiency (EQE) extracted from the I_{ph} data. **h** Temporal photovoltaic photoresponse of the device measured at 458 nm, exhibiting a rise 599 time (τ_r) of 1.56 μs and a decay time (τ_d) of 1.36 μs.

doped/pristine WSe_2 homojunction. Figure 6g, h present an input grayscale image (256 × 256 pixels and 8-bit depth)[51] and the corresponding processed outputs, respectively. Each pixel intensity (0-255) is linearly mapped to an incident optical power P_{in}. A 3 × 3 convolution kernel is implemented by assigning specific V_G to individual devices, defining a corresponding responsivity matrix R_{ij}. The output I_{ph} is calculated as $I_j = \sum R_{ij} \times P_{ij}$ following Kirchhoff's current law in a crossbar configuration. The sign of R_{ij} arises intrinsically from gate-induced reversal of band bending, which inverts the direction of photocarrier drift. Using the experimentally measured responsivity-gate-voltage relationship, standard image-processing functions, including edge detection and image sharpening, are successfully implemented, demonstrating simultaneous optical sensing and preprocessing at the device level.

Conclusions

In summary, we demonstrate that substitutional V doping is an effective and thickness-tolerant strategy for achieving p-type modulation in multilayer WSe_2 and for enabling homojunction-based electronic and optoelectronic devices. Controlled vanadium incorporation via CVT allows the formation of well-defined homojunctions with pristine WSe_2 across a wide thickness range. Leveraging this capability, we realize three representative device architectures: flexible photovoltaic devices, complementary CMOS-like inverters, and gate-tunable homojunction devices for in-sensor imaging. The flexible photovoltaic devices exhibit broadband photodetection with a high responsivity of 155.31 mA W^{-1}, a peak external quantum efficiency of 51.3%, and fast response times down to 1.56 μs, highlighting efficient photocarrier separation enabled by the V-induced p–n homojunction. In parallel, CMOS-like inverters demonstrate reliable complementary logic operation, while gate-tunable homojunctions enable reversible switching between positive and negative I_{ph} responses for programmable in-sensor image processing. These results establish V doping as a robust approach for carrier polarity control in multilayer WSe_2 and underscore its potential for integrated, multifunctional device architectures based on 2D semiconductors.

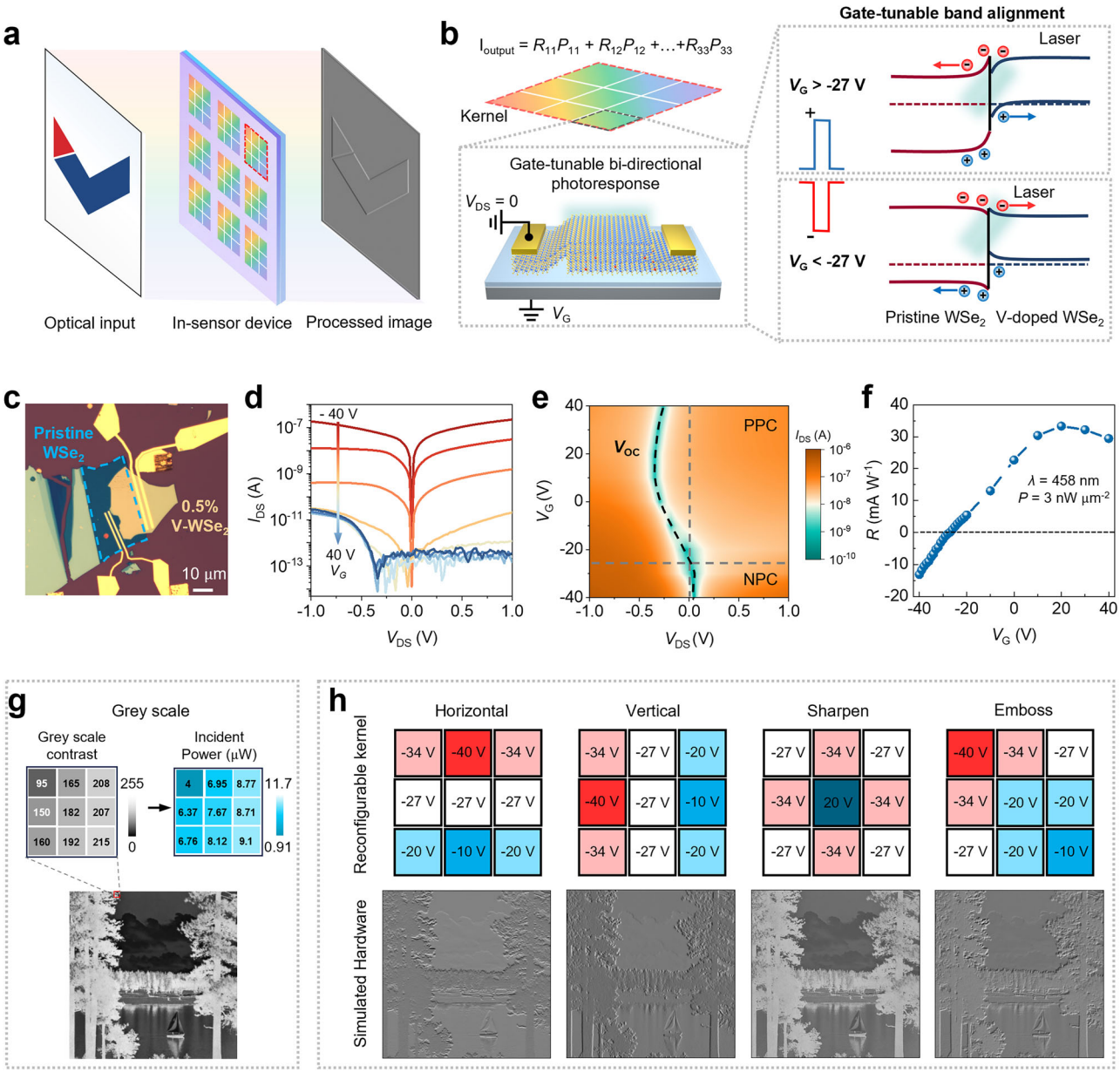


Fig. 6 | Gate-programmable in-sensor imaging based on a pristine/V-doped WSe_2 homojunction. a Schematic illustration of the in-sensor imaging concept, in which a gate-tunable homojunction device enables simultaneous optical sensing and signal preprocessing. **b** Gate-controlled band-alignment modulation at the pristine/V-doped WSe_2 homojunction, enabling reversible switching between NPC and PPC states and allowing each device to function as a programmable pixel within a convolution kernel. **c** Optical microscopy image of the fabricated 0.5% V-doped/pristine WSe_2 homojunction device. **d** Semilogarithmic output characteristics measured under dark conditions at V_G ranging from −40 to 40 V, showing gate-tunable diode behavior and reversible rectification. **e** Output characteristics under 458 nm illumination measured at $V_{DS} = 0$ V, revealing a gate-controlled transition between NPC and PPC, with the dashed line indicating the open-circuit voltage. **f** Gate-dependent photoresponsivity extracted from the I_{ph} measured at $V_{DS} = 0$ V, showing a sign reversal near the programming voltage. **g** Input grayscale image used for in-sensor image processing. **h** Simulated in-sensor image processing results, including edge detection and image sharpening, based on experimentally measured gate-programmable photoresponsivity of the homojunction device.

Methods

Single crystal synthesis

A single crystal of V-doped WSe_2 was synthesized by a two-step CVT process using iodine as a transport agent. The first step is the growth of a polycrystalline sample, followed by the second step for the single crystal growth. Highly pure reactant powders of tungsten (99.999%, Sigma Aldrich), selenium (99.998%, Sigma Aldrich), and vanadium (99.99%, Sigma Aldrich) were mixed and ground uniformly in an atomic ratio of $V_xW_{1-x}Se_2$ by weight. The V concentration denotes the nominal V: W precursor ratio before material synthesis. The mixed powder was compressed into a pellet, loaded into quartz ampules, sealed under high vacuum, and annealed at 1000 °C for 24 h. The polycrystalline powder was collected and resealed after iodine was added as a transport agent. The temperatures of the cold and hot ends were 950 °C and 1050 °C, respectively, and were maintained for over 200 h to facilitate sufficient diffusion and stabilization for the single crystal growth. The pristine sample was processed similarly, except that the reactant powders used were of tungsten and selenium only. The dopant concentration is calculated based on the initial precursor mass under the assumption of complete decomposition and incorporation into the reaction, following established practices in TMDs growth studies[52,53].

Device fabrication

Flexible photovoltaic device on mica substrate. Multilayer pristine WSe_2 and V-doped WSe_2 crystals were first mechanically exfoliated onto polydimethylsiloxane (PDMS) stamps. Selected flakes were subsequently transferred into flexible mica substrates using a dry transfer process assisted by optical microscope alignment. The pristine WSe_2 layer was transferred first, followed by the V-doped WSe_2 to form the homojunction structure. After stack assembly, Au electrodes (150 nm) were placed onto the device using a probe-tip-assisted transfer technique[54], enabling electrical contact without exposing the active layers to lithographic processing.

Homojunction devices on Si/SiO_2 (285 nm) substrate. First, the pristine and V-doped WSe_2 flakes were mechanically exfoliated onto SiO_2/Si substrates. Afterwards, multilayer pristine WSe_2 flakes were exfoliated onto PDMS and subsequently transferred onto selected V-doped WSe_2 flakes using a dry transfer system under optical microscope guidance to ensure accurate alignment. Electrical contacts were then defined by electron-beam lithography, followed by thermal evaporation of Cr/Au (5/50 nm) metal electrodes and standard lift-off processing.

Material and device characterizations

Raman results were obtained by using a commercial NT-MDT system equipped with a 532 nm excitation laser. XPS; K-Alpha, ThermoFisher Scientific, was employed to determine the elemental composition and chemical states. AFM and KPFM measurements were carried out using Park Systems NX10. TEM and STEM analyses were conducted using a JEOL JEM-ARM300CF 200 kV. Electrical transport, response speed, and I_{ph} measurements of the fabricated devices were performed using a Keysight B1500A parametric semiconductor device analyzer and a Keithley 2634B source measurement unit. Laser sources at 375, 458, 532, 642, 811, 942, and 1062 nm wavelengths were used for optoelectronic characterization, with a beam diameter of approximately 1 mm. The incident optical power density was calibrated using a PD300-BB silicon photodetector coupled to a Nova II power meter, with a 20 μm pinhole.

Data availability

The data that support the findings of this study are available from the corresponding author upon reasonable request.

Received: 9 February 2026; Accepted: 22 May 2026;
Published online: 28 May 2026

References

1. Hu, Y., Gao, Z., Luo, Z. & An, L. Next-generation image sensors based on low-dimensional semiconductor materials. *Adv. Mater.* **37**, e2501123 (2025).
2. Li, N. et al. 2D semiconductor-based optoelectronics for artificial vision. *Adv. Funct. Mater.* **33**, https://doi.org/10.1002/adfm.202305589 (2023).
3. Han, J. et al. 2D materials-based photodetectors with bi-directional responses in enabling intelligent optical sensing. *Adv. Funct. Mater.* **35**, https://doi.org/10.1002/adfm.202423360 (2025).
4. Hong, C., Tao, Y., Dat, V. K. & Kim, J.-H. Silicon photodiode-competitive 2D vertical photodetector. *npj Flex. Electron.* **9**, 13 (2025).
5. Kim, K. H. et al. High-efficiency WSe(2) photovoltaic devices with electron-selective contacts. *ACS Nano* **16**, 8827–8836 (2022).
6. Wang, H. et al. Van der Waals integration based on Two-dimensional materials for high-performance Infrared photodetectors. *Adv. Funct. Mater.* **31**, 2103106 (2021).
7. Yun, S. J. et al. Van der Waals multilayered films: Wafer-scale synthesis and applications in electronics and optoelectronics. *Adv. Funct. Mater.* https://doi.org/10.1002/adfm.202409458 (2024).
8. Qin, B. et al. Interfacial epitaxy of multilayer rhombohedral transition-metal dichalcogenide single crystals. *Science* **385**, 99–104 (2024).
9. Zhou, C. et al. Carrier type control of WSe_2 field-effect transistors by thickness modulation and MoO_3 layer doping. *Adv. Funct. Mater.* **26**, 4223–4230 (2016).
10. Dat, V. K. et al. Van der Waals integration of 1D Nb_2Pd_3Se8 and 2D WSe_2 for gate-tunable in-sensor image processing. *Adv. Mater.* **37**, e00011 (2025).
11. Oh, S. et al. Ultimate scaling of the metal-MoS_2 interface achieving high performance nanoscale schottky diodes via conductive atomic force microscopy. *Small* **21**, e2411380 (2025).
12. Palacios-Berraquero, C. et al. Atomically thin quantum light-emitting diodes. *Nat. Commun.* **7**, 12978 (2016).
13. Dat, V. K. et al. Gate-controlled multispectral response in graphene-based heterostructure photodetector. *Adv. Electron. Mater.* **10**, 2300517 (2024).
14. Li, Y. et al. Measurement of the optical dielectric function of monolayer transition-metal dichalcogenides:MoS_2,$MoSe_2$,WS_2, and WSe_2. *Phys. Rev. B* **90**, 205422 (2014).
15. Wang, H. et al. Approaching the external quantum efficiency limit in 2D photovoltaic devices. *Adv. Mater.* **34**, e2206122 (2022).
16. Zou, Y. et al. High-temperature flexible WSe_2 photodetectors with ultrahigh photoresponsivity. *Nat. Commun.* **13**, 4372 (2022).
17. Massicotte, M. et al. Picosecond photoresponse in van der Waals heterostructures. *Nat. Nanotechnol.* **11**, 42–46 (2016).
18. Hong, C. et al. Engineering electrode interfaces for telecom-band photodetection in MoS_2/Au heterostructures via sub-band light absorption. *Light. Sci. Appl.* **12**, 280 (2023).
19. Zhang, S. et al. High-sensitive ultrabroad photodetector based on $PtSe_2/WSe_2/PtSe_2$ van der Waals heterostructure. *Adv. Opt. Mater.* **13**, 2500127 (2025).
20. Nassiri Nazif, K. et al. High-specific-power flexible transition metal dichalcogenide solar cells. *Nat. Commun.* **12**, 7034 (2021).
21. Wen, B. et al. Ultrahigh-response of WSe_2 homojunction photodetectors induced by ferroelectric domains in periodically poled lithium niobate. *Adv. Funct. Mater.* e19097, https://doi.org/10.1002/adfm.202519097 (2025).
22. Liu, D. et al. WSe_2 Interdigitated p-n homojunction for broadband high-performance imaging detection through localization effect synergizes. *Adv. Funct. Mater.* e31930, https://doi.org/10.1002/adfm.202531930 (2026).
23. Nguyen, M. C. et al. High–performance polarity–reconfigurable transistor and photodiode via asymmetric transferred Schottky and evaporated ohmic contacts. *Adv. Funct. Mater.* e27192, https://doi.org/10.1002/adfm.202527192 (2025).
24. Jiang, Y., Chen, S., Zheng, W., Zheng, B. & Pan, A. Interlayer exciton formation, relaxation, and transport in TMD van der Waals heterostructures. *Light. Sci. Appl.* **10**, 72 (2021).
25. Pedersen, T. G., Latini, S., Thygesen, K. S., Mera, H. & Nikolić, B. K. Exciton ionization in multilayer transition-metal dichalcogenides. *N. J. Phys.* **18**, https://doi.org/10.1088/1367-2630/18/7/073043 (2016).
26. Leisgang, N. et al. Giant Stark splitting of an exciton in bilayer MoS_2. *Nat. Nanotechnol.* **15**, 901–907 (2020).
27. Fang, H. & Hu, W. Photogating in low dimensional photodetectors. *Adv. Sci.* **4**, 1700323 (2017).
28. Kumar, R. et al. Substitutional doping of 2D transition metal dichalcogenides for device applications: Current status, challenges and prospects. *Mater. Sci. Eng. R: Rep.* **163**, 100946 (2025).
29. Xu, D. et al. Vanadium metal doping of monolayer MoS_2 for p-type transistors and fast-speed phototransistors. *ACS Appl. Mater. Interfaces* **16**, 23771–23779 (2024).
30. Pan, Y. et al. Precise p-type and n-type doping of two-dimensional semiconductors for monolithic integrated circuits. *Nat. Commun.* **15**, 9631 (2024).

31. Ko, K. et al. Competition between bipolar conduction modes in extrinsically p-doped MoS_2: Interaction with gate dielectric matters. *ACS Nano* **19**, 1630–1641 (2025).
32. Vu, V. T. et al. Synthesis of $NbSe_2$/Bilayer Nb-Doped WSe_2 heterostructure from exfoliated WSe2 flakes. *Small Struct.* **5**, 2300401 (2024).
33. Zhang, K. et al. Tuning the electronic and photonic properties of monolayer MoS_2 via in situ rhenium substitutional doping. *Adv. Funct. Mater.* **28**, 1706950 (2018).
34. Pavoni, E. et al. First principles study of WSe2 and the effect of V doping on the optical and electronic properties. *Mater. Adv.* **5**, 2230–2237 (2024).
35. Kozhakhmetov, A. et al. Controllable p-type doping of 2D WSe_2 via vanadium substitution. *Adv. Funct. Mater.* **31**, 2105252 (2021).
36. Do, V. D. et al. Current rectification in a sub-2 nm CNT/*V*-doped WS_2/MoS_2CNT vertical monolayer P-N diode. *ACS Nano* **20**, 522–532 (2026).
37. Le, X. P. et al. High-performance p-type quasi-ohmic of WSe_2 transistors using vanadium-doped WSe_2 as intermediate layer contact. *ACS Appl. Mater. Interfaces* **16**, 52645–52652 (2024).
38. Nisi, K. et al. Defect-engineered magnetic field dependent optoelectronics of vanadium doped tungsten diselenide monolayers. *Adv. Optical Mater.* **10**, 2102711 (2022).
39. Nguyen, L.-A. T. et al. Spin-selective hole–exciton coupling in a V-doped WSe2 ferromagnetic semiconductor at room temperature. *ACS Nano* **15**, 20267–20277 (2021).
40. Yun, S. J. et al. Ferromagnetic order at room temperature in monolayer WSe2 semiconductor via vanadium dopant. *Adv. Sci.* **7**, 1903076 (2020).
41. Fan, S., Yun, S. J., Yu, W. J. & Lee, Y. H. Tailoring quantum tunneling in a vanadium-doped WSe2/SnSe2 heterostructure. Advanced. *Science* **7**, 1902751 (2020).
42. Pham, Y. T. H. et al. Tunable ferromagnetism and thermally induced spin flip in Vanadium-doped tungsten diselenide monolayers at room temperature. *Adv. Mater.* **32**, 2003607 (2020).
43. Sahoo, K. R. et al. Vanadium doped magnetic MoS_2 monolayers of improved electrical conductivity as spin-orbit torque layer. *Adv. Funct. Mater.* **35**, 2502408 (2025).
44. Gao, B. et al. Electrical polarity modulation in V-doped monolayer WS_2 for homogeneous CMOS inverters. *Small* **20**, e2402217 (2024).
45. Fan, S., Yun, S. J., Yu, W. J. & Lee, Y. H. Tailoring quantum tunneling in a vanadium-doped WSe_2/$SnSe_2$ heterostructure. *Adv. Sci.* **7**, 1902751 (2020).
46. Das, M. et al. High-performance p-type field-effect transistors using substitutional doping and thickness control of two-dimensional materials. *Nat. Electron.* **8**, 24–35 (2024).
47. Wang, F., Pei, K., Li, Y., Li, H. & Zhai, T. 2D homojunctions for electronics and optoelectronics. *Adv. Mater.* **33**, e2005303 (2021).
48. Shin, J. C. et al. Band structure engineering of wse2 homo-junction interfaces via thickness control. *Adv. Mater. Interfaces* **9**, https://doi.org/10.1002/admi.202101763 (2021).
49. Zhang, Y. et al. An ultrafast WSe_2 photodiode based on a lateral p-i-n homojunction. *ACS Nano* **15**, 4405–4415 (2021).
50. Shim, J. et al. Phosphorene/rhenium disulfide heterojunction-based negative differential resistance device for multi-valued logic. *Nat. Commun.* **7**, 13413 (2016).
51. Signal and Image Processing Institute (USC-SIPI) Image Database <https://sipi.usc.edu/database/> (Univ. Southern California, accessed 24 March 2024).
52. Choi, S. H. et al. Is chemical vapor deposition of monolayer WSe_2 comparable to other synthetic routes? *APL Mater.* **11,**111124 (2023).
53. Jiang, J. et al. Probing giant Zeeman shift in vanadium-doped WSe_2 via resonant magnetotunneling transport. *Phys. Rev. B* **103**, 014441 (2021).
54. Hong, C., Dat, V. K., Nguyen, M. C., Yu, W. J. & Kim, J. H. Robust van der Waals metal mask for residue-free and all-solid 2D material engineering. *Adv. Funct. Mater.* **34**, 2407821 (2024).

Acknowledgements

This work was partially supported by the Center for Materials Innovation and Technology, VinUniversity. N.T.D acknowledges the Brain Pool (BP) Program, National Research Foundation of Korea (NRF), Grant No.: RS-2023-00264072. This research is funded by Phenikaa University under grant number PU2025-4-A-03. Q.L.V acknowledge fast track funding from VinUni under grant number VUNI.2223.FT07. W.J.Y acknowledges the supported by the National Research Foundation of Korea (NRF) grant funded by the Korean government (MSIT) (NRF-2023K2A9A2A06059788, NRF-2020R1A5A1019649, RS-2024-00439520, RS-2024-00439092, RS-2025-05682968).

Author contributions

V.K.D., M.C.N., H.P.D., and T.D.N. contributed equally to this work. V.K.D., M.C.N., H.P.D., and N.T.D. carried out device fabrication. V.K.D., M.C.N., N.T.D., C.H., K.K.K., S.C.L., and W.J.Y. performed electrical and optoelectronic measurements and analyzed the data. H.P.D. conducted the in-sensor image processing simulation. M.B., M.H.P., and T.D.N. synthesized the WSe_2 crystals via the CVT method and performed material characterization. M.C.N. and V.D.D. carried out electrode patterning and metal deposition. T.U.T. and D.H.L. performed the Raman spectroscopy measurements. V.K.D., M.C.N., T.D.N., H.P.D., Q.L.V., W.J.Y., T.D.N., and N.T.D. interpreted the results and wrote the manuscript. All authors contributed to the discussion of the results and reviewed the manuscript.

Competing interests

The authors declare no competing interests.

Additional information

Supplementary information The online version contains supplementary material available at https://doi.org/10.1038/s43246-026-01215-9.

Correspondence and requests for materials should be addressed to Woo Jong Yu, Tuan Dung Nguyen or Ngoc Thanh Duong.

Peer review information *Communications Materials* thanks Gil-Ho Kim and the other, anonymous, reviewer(s) for their contribution to the peer review of this work. A peer review file is available.

Reprints and permissions information is available at http://www.nature.com/reprints

Publisher's note Springer Nature remains neutral with regard to jurisdictional claims in published maps and institutional affiliations.

Open Access This article is licensed under a Creative Commons Attribution-NonCommercial-NoDerivatives 4.0 International License, which permits any non-commercial use, sharing, distribution and reproduction in any medium or format, as long as you give appropriate credit to the original author(s) and the source, provide a link to the Creative Commons licence, and indicate if you modified the licensed material. You do not have permission under this licence to share adapted material derived from this article or parts of it. The images or other third party material in this article are included in the article's Creative Commons licence, unless indicated otherwise in a credit line to the material. If material is not included in the article's Creative Commons licence and your intended use is not permitted by statutory regulation or exceeds the permitted use, you will need to obtain permission directly from the copyright holder. To view a copy of this licence, visit http://creativecommons.org/licenses/by-nc-nd/4.0/.

© The Author(s) 2026